International Journal of Computer Vision, 9:3, 213–230 (1992)

Recognizing Corners by Fitting Parametric Models

KARL ROHR
Arbeitsbereich Kognitive Systeme, FB Informatik, Universität Hamburg, Bodenstedtstr. 16, 2000 Hamburg 50, FRG

Received January, 1992. Revised June 23, 1992.

Abstract
The parametric model of a certain class of characteristic intensity variations in Rohr (1990, 1992), which is the superposition of elementary model functions, is employed to identify corners in images. Estimates of the searched model parameters characterizing completely single grey-value structures are determined by a least-squares fit of the model to the observed image intensities applying the minimization method of Levenberg-Marquardt. In particular, we develop an analytical approximation of our model in such a way that function values can be calculated without numerical integration. Assuming the blur of the imaging system to be describable by Gaussian convolution our approach permits subpixel localization of the corner position of the unblurred grey-value structures, that is, to reverse the blur of the imaging system. By fitting our model to the original as well as to the smoothed original-image cues can be obtained for finding out whether the underlying model is an adequate description or not. Results are shown for real image data.

1 What Is a Corner?

Because the usage of the term *corner* is not uniform in the literature we briefly explain what is meant by a corner in the current contribution. If in a 3D-scene at least two surfaces meet then we will speak of a *3D-edge*. A corner in the 3D-scene, that is, a *3D-corner*, is formed when at least two 3D-edges join together. Analogously, we will speak of *2D-edges* (*2D-corners*) if at least two surfaces (edges) meet in the (2D-)image, that is, the term *corner* is uniformly characterized in 2D and 3D. Corners are always a subset of edges.

Normally, 3D-edges (3D-corners) are transformed to 2D-edges (2D-corners). However, there are additional circumstances that may create 2D-edges or 2D-corners, for example, illumination effects or the presence of occlusions (e.g., a T-junction is created if one 3D-edge occludes another). Therefore it may be advantageous to define a 2D-corner in the image plane and not by reasons of object constellations in the 3D-scene. The characterization of corners above is identical to the definition of junctions as is customary in the literature, so in the following we will use the terms *junction* and *corner* synonymously. T-, Y-, and ARROW-junctions are also T-, Y-, ARROW-corners. In addition, we find it more favorable to define corners in terms of joining edges as above than in terms of adjacent surfaces, because the number of adjacent surfaces in general does not discriminate between normal edges and corners. Surely, if three or more surfaces meet then there will always be a corner. However, when two surfaces meet it is not clear whether there is just a normal edge or an L-corner. Furthermore, since edges and corners always have a certain extent, the terms *edges* and *corners* will denote areas of image surfaces forming such features. In the 3D-scene this is because transitions cannot be ideally sharp (although here we will assume that they are ideally sharp or at least very sharp). Since imaging systems are bandlimited it is even more true that transitions in the image are extended. If we mean certain positions of features we will speak of edge points, edge lines, or corner points. Throughout this contribution the terms edge and corner will denote features in the image (i.e., 2D-edges and 2D-corners). Edges and corners in the 3D-scene are explicitly termed 3D-edges and 3D-corners.

2 Some Problems in Recognizing Corners

When trying to recognize characteristic (prominent) intensity variations in images with a computer vision system we are faced with a series of problems. Of special interest is the accurate determination of the position of corners, since small errors in the image plane in general lead to significant errors in a 3D-interpretation (c.f. figure 1), that is, the more precisely prominent features are derived from images the more reliably can (in principle) objects in the depicted 3D-scene be described. Consider for example a Y-junction. A (local) direct corner detector will perhaps yield the image position marked by a square in figure 2 which seems to be reasonable. If we first detect edge points, link them together on some kind of continuity assumption, and fit them by straight lines (supposing that the contours of the considered image are essentially straight lines) we may get the edge lines in figure 3. The first thing we can observe is that the edges are interrupted. The reason for the gaps is the underlying 1D-model of the edge detector, which is inadequate when it is applied to 2D-features. In addition, we see that while the extension of two of the three edge lines seem to intersect in one point, which could be considered to be the corner point, the third edge line (on the left side of the image) does not support this hypothesis very well. In order to cope with the uncertainties of the three edge lines one could determine the position of the corner point by minimizing the distance of the three edge lines to the searched intersection point. Although this would probably also yield a plausible estimate, the information of the intensities is not incorporated during the minimization process. The same holds true when both the results of the direct corner detector and of the edge detector would be combined to evaluate the position of the corner point.

The problems in determining the position of characteristic intensity variations as illustrated above has many reasons. One reason is that intensity structures can be very complex and because of the many factors having an influence on their generation the range of variations is very broad. Another difficulty stems from the fact that every imaging system is bandlimited. So, image structures are always blurred. In addition, reducing the amount of noise contaminating the recorded signal by applying filters leads to a further blurring. Each blurring is in general accompanied by a displacement of prominent structures in the image plane.

Consider for example figure 4, which shows a qualitative sketch of localization properties of different approaches applied to detect L-corners. The locus of

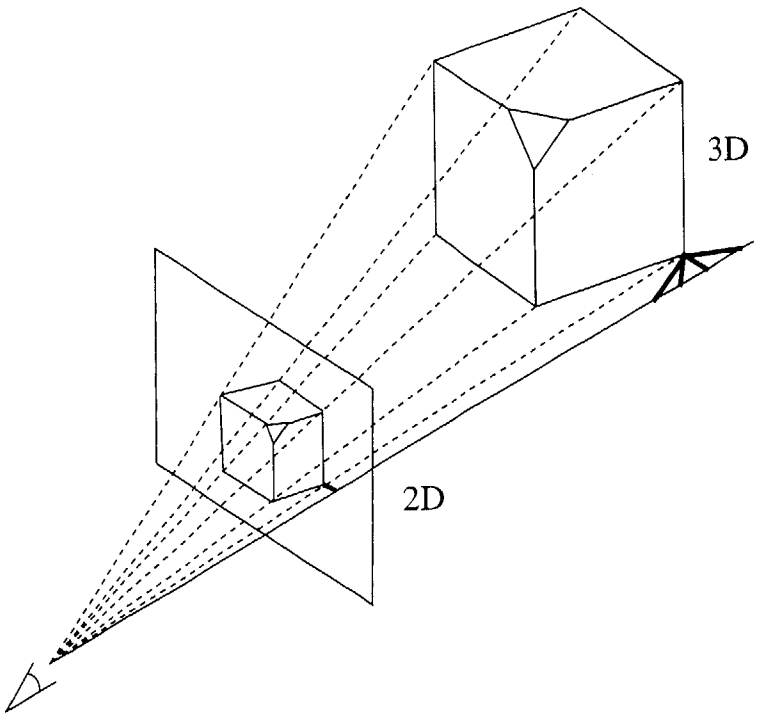

Fig. 1. Transformation of a polyhedral object onto the image plane.

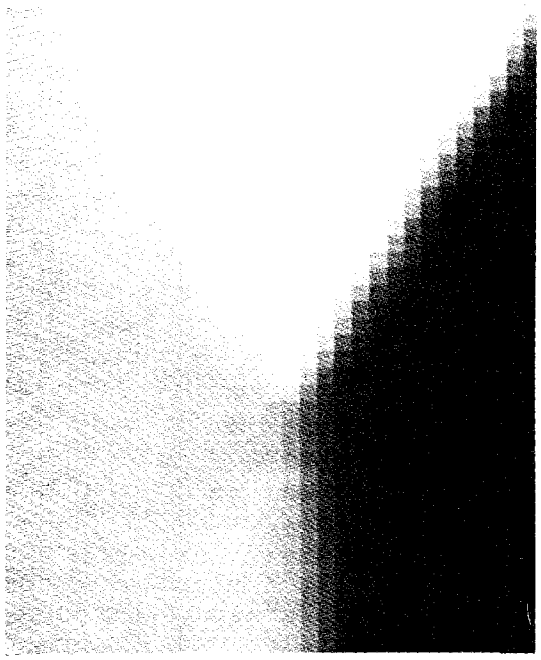

Fig. 2. Result of a direct corner detector.

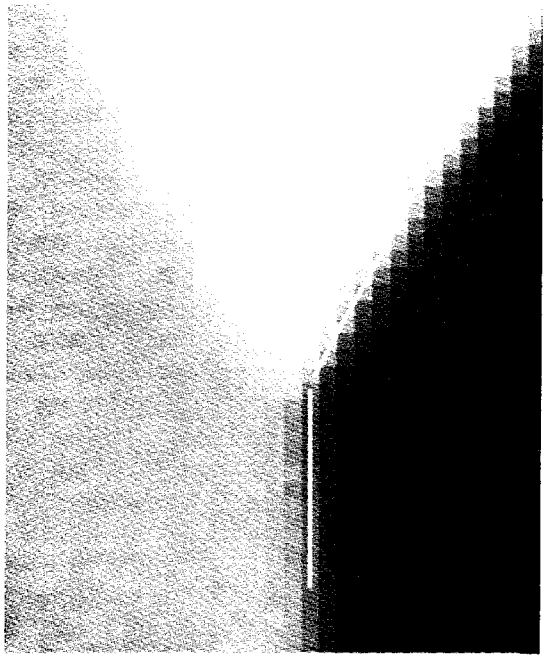

Fig. 3. Result of an edge detector.

points having steepest slope between the two adjacent regions is characterized by the dashed line. Direct corner detectors define the corner point at the position of

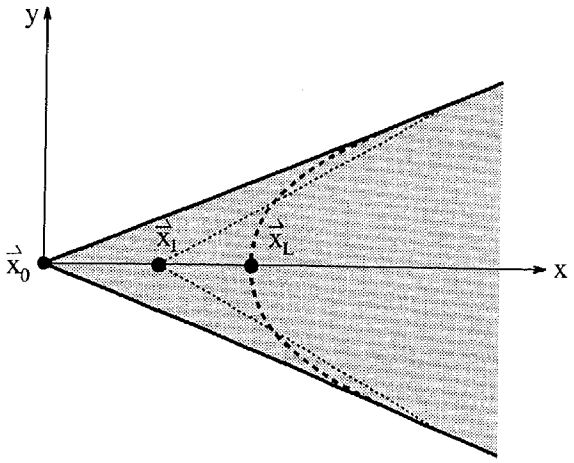

Fig. 4. Qualitative sketch of results of different approaches for detecting L-corners.

maximal planar curvature in this line ($\vec{x}_L$). The same position is searched for by indirect methods that first detect edge points, link them together, and then identify the corner point with the local curvature extrema on this contour chain. Approximating the contour chains by straight lines and intersecting those lines yields (qualitatively) the position $\vec{x}_1$ which in general lies between $\vec{x}_0$ and $\vec{x}_L$ since the detected edge points in the vicinity of the corner lie inside the depicted sector and straight line approximation and intersection yields a position on the left of $\vec{x}_L$.

If, instead, we suppose objects in the depicted 3D-scene to have ideal sharp 3D-edges and we assume the imaging system not to introduce blur, then the contour of the L-corner should result in the solid straight line. In this case, the searched corner point is localized at the position $\vec{x}_0$. When more complex junctions, such as *T*-, *Y*- or ARROW-corners are considered, the localization of corner points becomes more difficult.

3 Related Literature

In the previous section we mentioned that edge detectors assuming 1D grey-value transitions (e.g., Canny 1986) in general have difficulties in the vicinity of corners. An approach to reverse the blur of filter operations is introduced in Bergholm (1987). He tracks edge points from coarse to fine image resolution in order to reduce the noise and at the same time diminish the displacement of edges. However, at corners there are still gaps. Other approaches try to improve the edges

near corners by filling the gaps with additional edge points (Korn 1988; Li et al. 1989; Beymer 1991) which is not always satisfactory. All the approaches above rely on the maximum of the gradient in the direction of the gradient ("directional gradient") which for an L-corner leads to the position $\vec{x}_L$ and not to the position $\vec{x}_0$ we are searching for (see figure 4), that is, the problem of the displacement of corners depending on the blur of the imaging system is not addressed. An alternative approach for detecting edges is the use of the Laplacian-of-Gaussian (LoG) (see Marr & Hildreth 1980). Although this operator leads to edges swinging around L-corners (see figure 5) the detected edge lines exactly pass through the corner position $\vec{x}_0$, independently of the amount of filtering (see Berzins 1984). Qualitatively, the position $\vec{x}_2$ is found when edge points extracted with the LoG are approximated by straight lines. A comparison of detected edges by the "directional gradient" and the LoG for a Y-corner can be found in De Micheli et al. (1989).

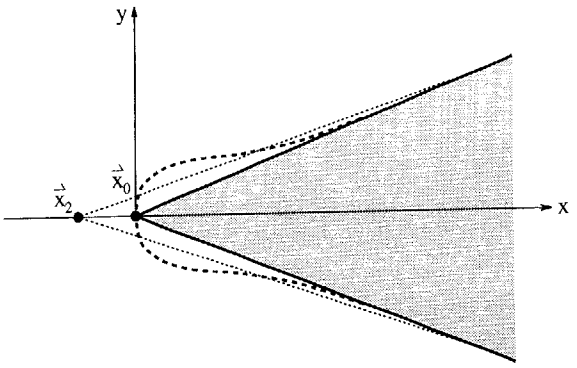

Fig. 5. Using the Laplacian-of-Gaussian (LoG) for detecting L-corners.

Direct corner detectors search the position $\vec{x}_L$, where in general no attempt is made to reverse the blur of the imaging system in order to find the position $\vec{x}_0$ (e.g., Dreschler & Nagel 1981; Kitchen & Rosenfeld 1982; Zuniga & Haralick 1983; Förstner 1986; Noble 1987; Rangarajan et al. 1989). Although an L-junction often serves as the only model for the corner detector the obtained operator is applied onto the whole image (i.e., for more complex corners, too). An approach combining the properties of direct corner detectors and the localization behavior of the LoG for L-junctions can be found in Deriche and Giraudon (1990). In Giraudon and Deriche (1991) an extension to trihedral corners is reported. Their approach relies on local maxima of the determinant of the Hessian matrix (Beaudet 1978) which are tracked across different image scales. One problem is that for a trihedral corner the number of local maxima depends on the heights of the different intensity plateaus. For more complex corners (e.g., 4 edge lines joining in one point) the constellations and therefore the tracking of local maxima in scale space will become even more difficult. Thus, this approach can hardly be generalized in a straightforward way. The direct corner detectors above only determine the position of corners. In contrast to this, Guiducci (1988) estimates additional attributes for L-corners (angle of aperture, height, and smoothness). However, no attempt is made to estimate the position $\vec{x}_0$ for an L-corner nor to extend this approach to more complex corners.

4 Outline of Our Approach

Here, we favor an approach, which in order to estimate the position as well as additional attributes of corners, fits a parametric model of a certain class of prominent features directly to observed intensity variations. This approach is not limited to L-corners but comprises step edges and more complex corners, such as T-, Y-, ARROW-corners, and all other junction types represented in the labeling system of Waltz (1975). But of what use is a quantitative model? First of all, in bringing in a-priori knowledge the underlying assumptions are made explicit, which opens the possibility to check whether the assumptions are fulfilled in the image (e.g., to find out if the model for a single grey-value structure is inadequate or whether there are interaction effects from other grey-value structures). On the other hand, we are able to derive analytical expressions—for example, for the displacement of the corner position when applying Gaussian filters of different size (see section 5.4).

For our investigation we assume polygonal objects in the depicted scene to have ideal (or very) sharp 3D-edges. The blur of the imaging system should be describable by Gaussian convolution, and the noise introduced in the recording process is supposed to be additive, independent of the signal, and normally distributed with zero mean. If we further assume no specularities and interreflections then the structural intensity variations of corners can be described by smoothed ideal wedge-shaped structures having symmetric transitions between each two adjacent regions. The considered features should also be well isolated and taken with sufficient image resolution. Although

these assumptions at first glance seem to be very restrictive it is otherwise not clear that we actually get the measurements we want. This holds true for most of the existing approaches for feature extraction. A relaxation of the restrictions should be the next step.

For recovering corners, our approach explicitly utilizes a model describing 2D intensity variations. If the underlying assumptions are fulfilled then we can reverse the blur of the imaging system. Independent of the complexity of corners—that is, the number of joining edges—we here have a possibility to find the origin (up to subpixel resolution) of the unsmoothed ideal grey-value structures (for the L-corner in figure 4 this is the position $\vec{x}_0$). Moreover, if, in order to reduce the noise, we first smooth the image with a Gaussian filter we get this position, too. This localization property in particular is important when the distances of object parts to the camera differ very much. Then a corner in the front, for example, is represented by a relatively large number of pixels compared to a corner in the rear. The blur of a corner in the front will be more pronounced and therefore the displacement of the corner positions in general will be different. If these different displacements are not compensated, a 3D-reconstruction incorporating these measurements in general cannot be supposed to be very reliable. In addition to the determination of the position of corners to subpixel resolution we also estimate additional properties of corners, such as the characterizing angles, the heights of intensities, and the amount of blur. Initial values for the model parameters are found by local operators. Thus, we address both the problem of detection and localization. Obviously, by fitting the parametric model to single features, the structural information of the intensities is taken into account. Moreover, we sketch a unifying framework for recognizing edges and corners of a certain class. Extensions of this class are (in general) straightforward.

An overview of our approach is sketched in figure 6. In order to find corners in the image we first apply a local operator to detect points of high image variations. Then, inside an area around each detected corner we determine straight lines and, depending on the number of these edge lines, a parametric model is selected to be fitted to the intensities. Here, the size of the considered area was chosen interactively to about 25×25 pixels. Our current investigation assumes straight edges, that is, we do not treat curved edge lines. Surely, the detection of corner points and the determination of initial values for the parameters is a very hard part and we do not claim that we have solved this problem. But we feel that together with a quantitative model as ours this problem can be attacked in an effective way. The least-squares fit to individual features on one hand yields precise estimates of the searched parameters and on the other hand opens the possibility to check whether the identified model is a good description.

5 A General Parametric Model

Let the image coordinates and the set of unknown model parameters be denoted by $\vec{x} = (x, y)$ and $\vec{p} = (p_1, \ldots, p_n)$, respectively. Our general model $g_M(\vec{x}, \vec{p})$ for describing intensity variations of a certain class of corners is the superposition of model functions of the L-corner $g_{ML}(\vec{x}, \vec{p})$ (Rohr 1990, 1992).

$$g_M(\vec{x}, \vec{p}) = \sum_{i=0}^{N-1} g_{MLi}(\vec{x}, \vec{p}), \qquad N \geq 2 \quad (1)$$

Each function $g_{ML}(\vec{x}, \vec{p})$ is obtained by convolution of an ideal wedge shaped grey-value structure $E(\vec{x}, \vec{p})$ with a Gaussian filter $G(\vec{x}, \vec{p})$ (see later for details).

$$g_{ML}(\vec{x}, \vec{p}) = E(\vec{x}, \vec{p}) * G(\vec{x}, \vec{p}) \quad (2)$$

Using (1) we can model arbitrary complex grey-value structures in terms of the number of adjacent regions. The choice $N = 2$ specifies the intensity variations of a step edge or an L-corner. For $N = 3$ we obtain T-, Y-, and ARROW-corners. In the case of $N = 4$ we have PEAK, K-, X-, MULTI-, and XX-corners in the notation of the labeling system of Waltz (1975). For $N = 5$ KA- and KX-corners are formed, and $N \geq 6$ leads to even more complex grey-value structures. See figure 7 for an example of a K-corner model. The specific number of model parameters is $n = 3 + 2N$. The quantitative L-corner model of Berzins (1984) and the model of a trihedral junction of De Micheli et al. (1989) and Giraudon and Deriche (1991) are special cases of our general model.

5.1 Model Function of an L-Corner

In the local coordinate system (figure 8) an ideal wedge-shaped grey-value structure

$$E_{lok}(\vec{x}, \beta, a) = \begin{cases} a & \text{if } x \geq 0 \wedge \\ & |y| \leq \tan(\beta/2)x \\ 0 & \text{otherwise} \end{cases}$$

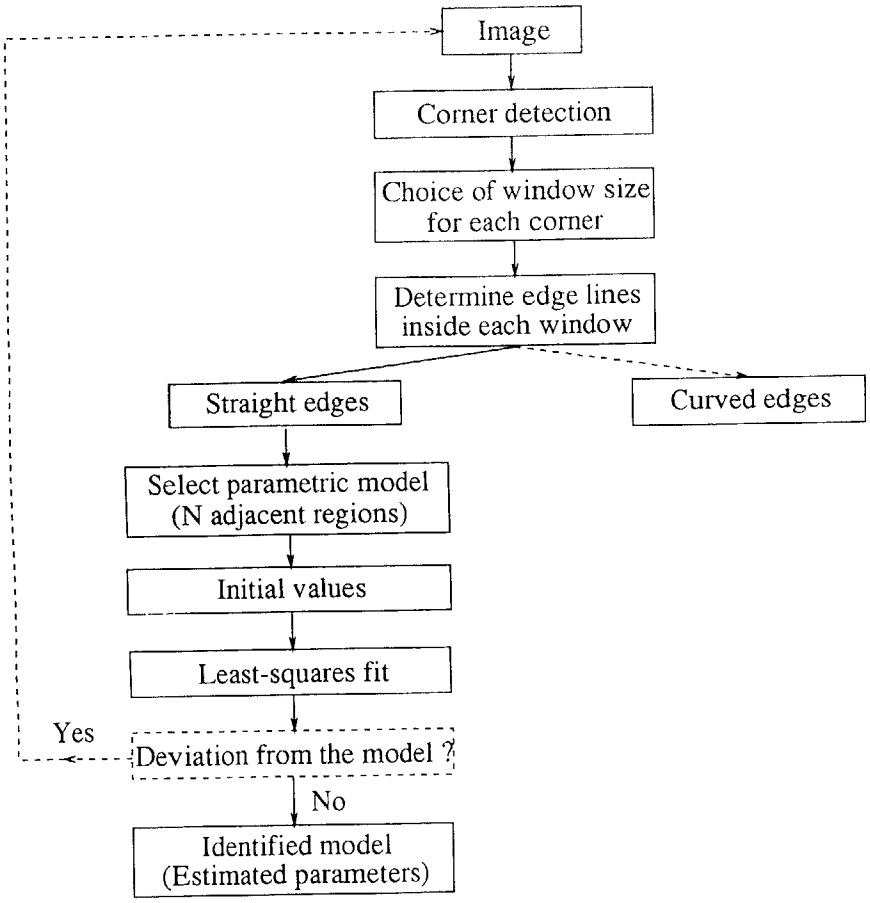

Fig. 6. Overview of our approach.

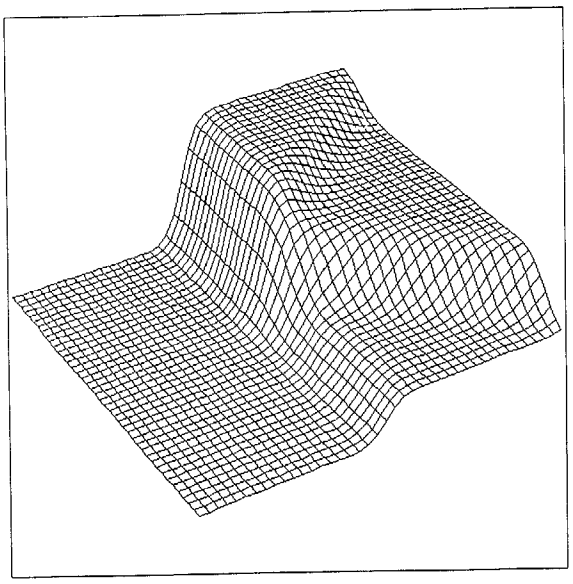

Fig. 7. Model of a K-corner.

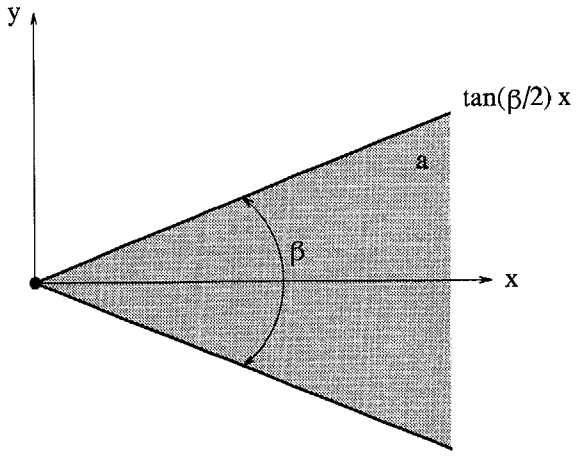

Fig. 8. L-corner in the local coordinate system.

with angle of aperture β and height a can be characterized by two parts, each having an angle of aperture $\beta/2$. The lower part is just a reflection of the upper part with

respect to the x-axis. Exploiting this symmetry leads to a model function valid in the whole range of $0° < \beta < 180°$. In contrast to this, Berzins (1984) derives three functions for an L-corner, the first valid for $0° < \beta < 90°$, the second for $\beta = 90°$ and the third for $90° < \beta < 180°$. Our model comprises these three functions and is the superposition of two of the first functions of Berzins. Moreover, more complex corners are also obtained by superposition of model functions of the L-corner.

Convolution of $E_{lok}(\vec{x}, \beta, a)$ with a 2D Gaussian filter

$$G(\vec{x}) = G(x)G(y), \qquad G(x) = \frac{1}{\sqrt{2\pi}} e^{-x^2/2}$$

leads with $\vec{\xi} = (\xi, \eta)$ to the model of the L-corner in the local coordinate system

$$g_{ML_{lok}}(\vec{x}, \beta, a) = E_{lok}(\vec{x}, \beta, a) * G(\vec{x})$$

$$= \int_{-\infty}^{+\infty} \int_{-\infty}^{+\infty} E_{lok}(\vec{\xi}, \beta, a) G(\vec{x} - \vec{\xi})\, d\vec{\xi}$$

Integration of $G(x)$ yields the Gaussian error function $\phi(x)$. Using $t = \tan(\beta/2)$, $\zeta_2 = tx - y$ and

$$\phi(x) = \int_{-\infty}^{x} G(\xi)\, d\xi$$

$$\phi(\vec{x}) = \phi(x)\phi(y)$$

$$D(\vec{x}) = G(x)\phi(y)$$

it follows for the upper part of the sector (up to the height a)

$$M(\vec{x}, \beta) = \int_{\xi=0}^{\infty} \int_{\eta=0}^{t\xi} G(\vec{x} - \vec{\xi})\, d\vec{\xi}$$

$$= \phi(\vec{x}) - m(\vec{x}, \beta) \tag{3}$$

where

$$m(\vec{x}, \beta) = \int_{-\infty}^{x} D(\xi, t\xi - \zeta_2)\, d\xi \tag{4}$$

Finally, with $\vec{x}^{\#} = (x, -y)$ and $\phi(-y) = 1 - \phi(y)$, the model function of an L-corner can be described as

$$g_{ML_{lok}}(\vec{x}, \beta, a) = a\big(M(\vec{x}, \beta) + M(\vec{x}^{\#}, \beta)\big)$$

$$= a\big(\phi(x) - m(\vec{x}, \beta) - m(\vec{x}^{\#}, \beta)\big)$$

$$0° < \beta < 180° \tag{5}$$

For $\beta = 180°$ we have the model of a step edge.

$$g_{MSK_{lok}}(\vec{x}, a) = a\, \phi(x)$$

The L-corner model in the absolute coordinate system (figure 9) is obtained by an additional translation of the local coordinate system by $\vec{x}_0 = (x_0, y_0)$ and a rotation by α. Including a scaling factor σ that characterizes the amount of blur introduced by the Gaussian filter these steps are defined by the following transformation. For convenience we explicitly write only the dependency on α.

$$\vec{x}^{*}(\alpha) = \left(\frac{(x - x_0)\cos(\alpha) + (y - y_0)\sin(\alpha)}{\sigma}, \right.$$

$$\left. \frac{-(x - x_0)\sin(\alpha) + (y - y_0)\cos(\alpha)}{\sigma} \right)$$

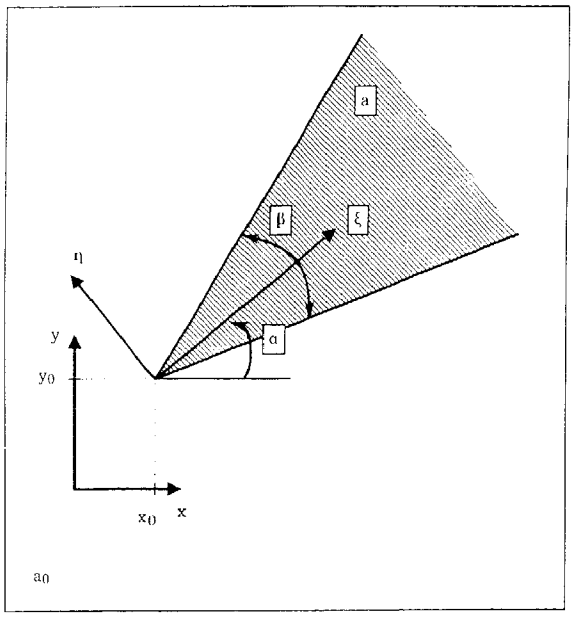

Fig. 9. L-corner in the absolute coordinate system.

In the general case the local parameters $\vec{p}_{lok} = (\vec{x}, \beta, a)$ are transformed by $\vec{h}(\vec{x}, \vec{p}) = \big(h_1(\vec{x}, \vec{p}), \ldots, h_4(\vec{x}, \vec{p})\big)$ where each local parameter is substituted by functions of the global parameters. Using $\vec{h}(\vec{x}, \vec{p}) = (\vec{x}^{*}(\alpha), \beta, a)$, the L-corner in the absolute coordinate system can be expressed as

$$g_{ML}(\vec{x}, \vec{x}_0, \alpha, \beta, a, \sigma) = g_{ML_{lok}}\big(\vec{h}(\vec{x}, \vec{p})\big) \tag{6}$$

5.2. Model Functions of General Corners

With (1) and (6) it follows that our general parametric model is describable by

$$g_M(\vec{x}, \vec{p}) = \sum_{i=0}^{N-1} g_{ML_i}(\vec{x}, \vec{p}) = a_0 + \sum_{i=1}^{N-1} g_{ML_{lok}}\left(\vec{h}_i(\vec{x}, \vec{p})\right), \quad N \geq 2 \quad (7)$$

where to the basic plateau a_0 a number of $N - 1$ model functions $g_{ML_{lok}}\left(\vec{h}_i(\vec{x}, \vec{p})\right)$ are added. In the case of 2 adjacent regions (step edge, L-corner) the model function is determined using

$$N = 2: \quad \vec{p} = (\vec{x}_0, \alpha, \beta_1, a_0, a_1, \sigma)$$
$$\vec{h}_1(\vec{x}, \vec{p}) = \left(\vec{x}^*(\alpha), \beta_1, a_1 - a_0\right)$$

It is also possible to construct this function by superposition of two model functions with angle of aperture β and $360° - \beta$, respectively. Below, we give the expressions needed for the cases of 3 adjacent regions (T-, Y-, ARROW-corners; see also figure 10) and 4 adjacent regions (PEAK-, K-, X-, MULTI-, and XX-corners), too. The number of the model parameters in these cases is 9 and 11.

$$N = 3: \quad \vec{p} = (\vec{x}_0, \alpha, \beta_1, \beta_2, a_0, a_1, a_2, \sigma)$$
$$\vec{h}_2(\vec{x}, \vec{p}) = \left(\vec{x}^*(\alpha - \beta_1/2 - \beta_2/2), \beta_2, a_2 - a_0\right)$$

$$N = 4: \quad \vec{p} = (\vec{x}_0, \alpha, \beta_1, \beta_2, \beta_3, a_0, a_1, a_2, a_3, \sigma)$$
$$\vec{h}_3(\vec{x}, \vec{p}) = \left(\vec{x}^*(\alpha - \beta_1/2 - \beta_2 - \beta_3/2), \beta_3, a_3 - a_0\right)$$

5.3 Partial Derivatives of the General Model

For both fitting the general model to intensity variations and the evaluation of analytical expressions we need the partial derivatives of $g_M(\vec{x}, \vec{p})$. At the position $(\vec{x}^\circ, \vec{p}^\circ)$ these derivatives are calculated using the generalized chain rule (e.g., Bronstein & Semendjajew 1981):

$$\left.\frac{\partial g_M(\vec{x}, \vec{p})}{\partial p_j}\right|_{(\vec{x}^\circ, \vec{p}^\circ)} = \frac{\partial a_0}{\partial p_j} + \sum_{i=1}^{N-1} \left(\sum_{l=1}^{4} \left.\frac{\partial g_{ML_{lok}}(\vec{p}_{lok})}{\partial p_{lok_l}}\right|_{\vec{h}_i(\vec{x}^\circ, \vec{p}^\circ)} \times \left.\frac{\partial h_{il}(\vec{x}, \vec{p})}{\partial p_j}\right|_{(\vec{x}^\circ, \vec{p}^\circ)} \right) \quad (8)$$

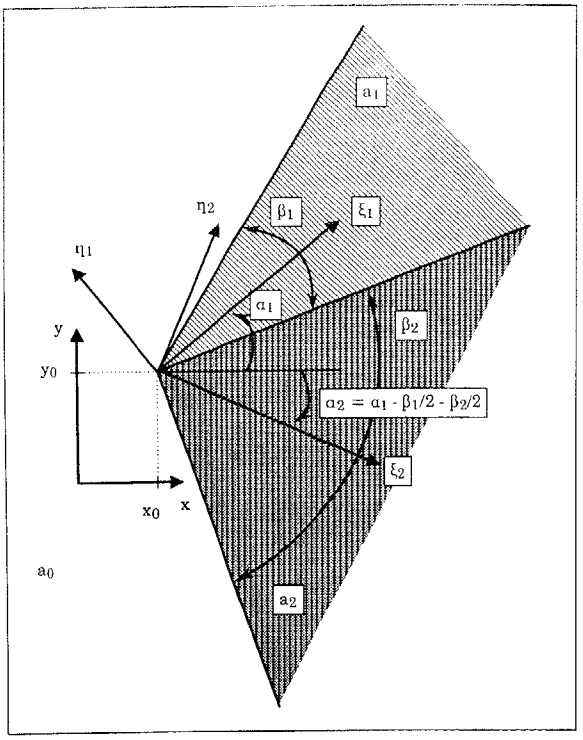

Fig. 10. 3 adjacent regions.

With the introduction of some symbols—$\zeta_1 = x + ty$, $\zeta_2 = tx - y$, $\zeta_1^\# = x - ty$, $\zeta_2^\# = tx + y$, $\vec{\zeta} = (\zeta_2/q, \zeta_1/q)$, $\vec{\zeta}^\# = (\zeta_2^\#/q, \zeta_1^\#/q)$, $q = \sqrt{1 + t^2}$—and incorporating the partial derivatives of $m(\vec{x}, \beta)$ from (4)

$$\frac{\partial m(\vec{x}, \beta)}{\partial x} = D(\vec{x}) - \frac{t}{q} D(\vec{\zeta})$$

$$\frac{\partial m(\vec{x}, \beta)}{\partial y} = \frac{1}{q} D(\vec{\zeta})$$

$$\frac{\partial m(\vec{x}, \beta)}{\partial \beta} = -\frac{1}{2}\left(G(\vec{x}) + \frac{\zeta_1}{q} D(\vec{\zeta}) \right)$$

we finally get the partial derivatives of $g_{ML_{lok}}(\vec{p}_{lok})$ needed in (8).

$$\frac{\partial g_{ML_{lok}}(\vec{p}_{lok})}{\partial x} = \frac{at}{q}\left(D(\vec{\zeta}) + D(\vec{\zeta}^\#)\right)$$

$$\frac{\partial g_{ML_{lok}}(\vec{p}_{lok})}{\partial y} = \frac{a}{q}\left(D(\vec{\zeta}^\#) - D(\vec{\zeta})\right)$$

$$\frac{\partial g_{ML_{lok}}(\vec{p}_{lok})}{\partial \beta} = a\left[G(\vec{x}) + \frac{1}{2q}\left(\zeta_1 D(\vec{\zeta}) + \zeta_1^\# D(\vec{\zeta}^\#)\right)\right] \quad (9)$$

$$\frac{\partial g_{ML_{lok}}(\vec{p}_{lok})}{\partial a} = \frac{1}{a} g_{ML_{lok}}(\vec{p}_{lok})$$

It should be noted that all partial derivatives with the exception of the derivative for the height a are expressed by the Gaussian function $G(x)$ and the Gaussian error function $\phi(x)$. For computing $\phi(x)$ we use a rational approximation found in Abramowitz and Stegun (1965) (see appendix I).

5.4. Displacement of the L-Corner Point

Having defined the general parametric model and calculated its partial derivatives we are able to evaluate the displacement of the L-corner point when blurring with a Gaussian filter. In figure 4 the position of the L-corner point was denoted by $\vec{x}_L$ and is searched for by direct corner detectors and indirect approaches determining the point of maximum curvature of linked edge points. It should be mentioned that the estimation of partial derivatives in grey-value images needed for the corner detectors above is also a filtering step, which leads to a further displacement of the corner position. However, assuming Gaussian blur, the filter effect of the imaging system and of the derivative operators is describable by an overall blur of σ' (see also section 8); then the following calculations remain true for this amount of blur.

The position $\vec{x}_L$ is located on the line with steepest grey-value slope given by $g_x^2 g_{xx} + 2g_x g_y g_{xy} + g_y^2 g_{yy} = 0$ (see, e.g., Canny 1986), where the subscripts to the picture function $g = g(\vec{x})$ stand for the partial derivatives in x- and y-direction. The second partial derivatives of our model according to (9) are

$$\begin{aligned}
\frac{\partial^2 g_{ML_{lok}}(\vec{p}_{lok})}{(\partial x)^2} &= \frac{at}{q^3}\left[2qG(\vec{x}) - t\left(\zeta_2 D(\vec{\zeta}) + \zeta_2^{\#} D(\vec{\zeta}^{\#})\right)\right] \\
\frac{\partial^2 g_{ML_{lok}}(\vec{p}_{lok})}{\partial x \partial y} &= \frac{at}{q^3}\left(\zeta_2 D(\vec{\zeta}) - \zeta_2^{\#} D(\vec{\zeta}^{\#})\right) \\
\frac{\partial^2 g_{ML_{lok}}(\vec{p}_{lok})}{(\partial y)^2} &= -\frac{at}{q^3}\left[2qG(\vec{x}) + \frac{1}{t}\left(\zeta_2 D(\vec{\zeta}) + \zeta_2^{\#} D(\vec{\zeta}^{\#})\right)\right] \qquad (10)
\end{aligned}$$

Since our L-corner model is symmetric to the x-axis the corner point is displaced along the line $y = 0$. We can now (numerically) calculate the position $\vec{x}_L = (x_L, 0)$ as the solution of the following implicit equation setting $x' = x/q$ (remember that $t = \tan(\beta/2)$ and $q = \sqrt{1 + t^2}$).

$$G(x') - t^2 x' \phi(x') = 0 \qquad (11)$$

From this equation we see that since $G(x') > 0$ and $\phi(x') > 0$ the solution will always be $x_L > 0$. For the displacement of the L-corner point in dependence of the model parameters β, a, σ, follows:

- $x_L(\beta)$ is given by a nonlinear relationship (see figure 11). For small angles of aperture β the variation of the displacement is larger than for large values of β. Theoretically there is no upper bound for the displacement. If $\beta = 90°$, for example, the calculated position is $x_L = 0.71567$. For $\beta = 180°$ (step edge) the displacement is zero.
- $x_L(a) = \text{const}$; the position of the corner point is independent of the heights of grey-value plateaus.
- $x_L(\sigma) = \text{const} \cdot \sigma$; there exists a linear relationship. Doubling the value of σ, for example, leads to twice the displacement of the position. For $\sigma \to 0$, the solution is $x_L \to 0$ and for $\sigma \to \infty$ we have $x_L \to \infty$.

Bergholm (1987), De Micheli et al. (1989), and Deriche and Giraudon (1990) also studied the displacement of the L-corner point. However, they did not derive an expression like the one in (11). Since our model is valid for $0° < \beta < 180°$, the derived results hold for this whole range, too.

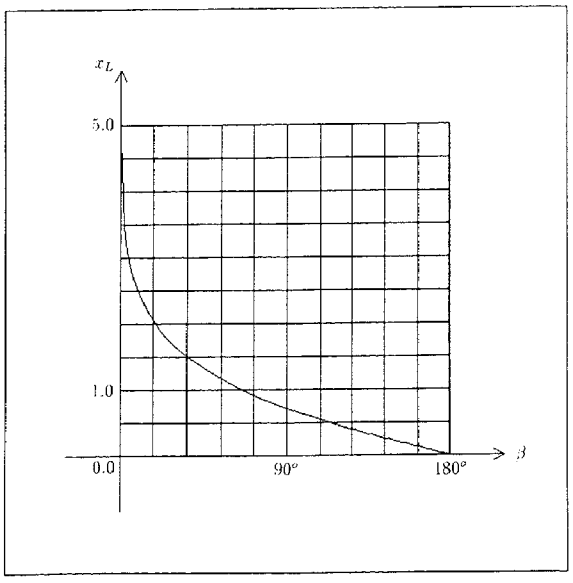

Fig. 11. Displacement of the L-corner point in dependence of the angle of aperture β.

6 An Approximation of the Parametric Model

In order to compute function values of the L-corner model $g_{ML_{lok}}(\vec{x}, \beta, a)$ in (5) we use a rational approximation of the ϕ-function. Still, there is an integral that cannot be evaluated in closed form. In our previous investigation, Rohr (1990, 1992), we integrated numerically. In this section, we introduce an approximation of the L-corner model in such a way that function values of the model can be calculated without numerical integration. This approximation exploits the fact that the Gaussian function $G(x)$ can very well be approximated by a cubic spline $B(x)$. Using the two auxiliary functions

$$B_1(x) = \frac{1}{6h}\left[1 + 3\left(\left(1 - \frac{x}{h}\right) + \left(1 - \frac{x}{h}\right)^2 - \left(1 - \frac{x}{h}\right)^3\right)\right]$$

$$B_2(x) = \frac{1}{6h}\left(2 - \frac{x}{h}\right)^3$$

the cubic spline is defined by $B(-x) = B(x)$ and

$$B(x) = \begin{cases} B_1(x) & 0 \le x \le h \\ B_2(x) & h \le x \le 2h \\ 0 & x \ge 2h \end{cases} \qquad (12)$$

Minimizing the squared difference between $G(x)$ and $B(x)$ (distance between the two functions with respect to the norm of L_2) for $\sigma = 1$ we found a value of $h = 1.67668$. For this value the difference function between $G(x)$ and $B(x)$ is displayed in figure 12. The magnitude of the largest deviation is smaller than $8 \cdot 10^{-3}$. Between general values of σ and h exists a linear relationship (see Rohr & Schnörr 1992). For $|x| \ge 2h$, $B(x)$ is equal to zero and for $|x| \le 2h$, $B(x)$ is described by third-order polynomials. The cubic spline is now used to substitute the Gaussian function under the integral in (4). For each interval in $|x| \le 2h$ the integrand then consists of the multiplication of a third-order polynomial with the ϕ-function. This integral, however, can be evaluated in closed form ($c_5 = c_1 + 2c_3$; $c_6 = c_2 + 3c_4$):

$$\int (c_1 + 2c_2\xi + 3c_3\xi^2 + 4c_4\xi^3)\phi(\xi)\, d\xi = (c_5 + c_6\xi + c_3\xi^2 + c_4\xi^3)G(\xi) + (-c_6 + c_1\xi + c_2\xi^2 + c_3\xi^3 + c_4\xi^4)\phi(\xi) \qquad (13)$$

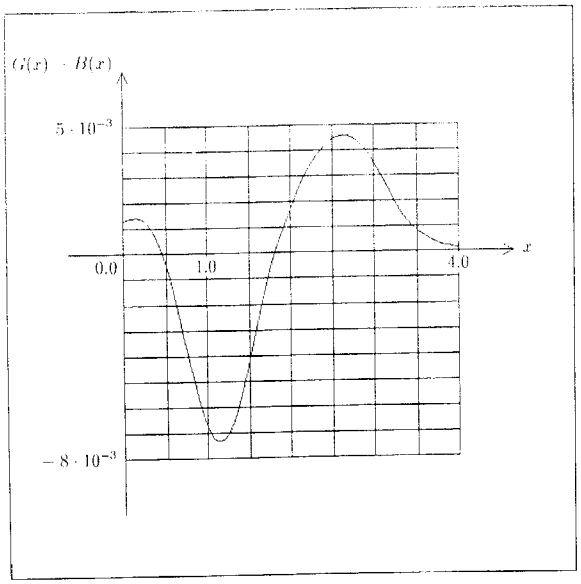

Fig. 12. Difference between Gaussian function and cubic spline.

With (13) we have explicit expressions for $m(\vec{x}, \beta)$ and $g_{ML_{lok}}(\vec{x}, \beta, a)$ in (4) and (5). The coefficients c_i for each of the four intervals are listed in appendix II. Using this approximation the general model function as well as all partial derivatives of it are given in terms of polynomials, $G(x)$ and $\phi(x)$.

Another approximation of the model function has been derived by Rohr and Schnörr (1992) whereby both Gaussian functions in (3) were replaced, each by a cubic spline. In our experiments it turned out that both approximations reduce the computation time to nearly the same extent. However, the approximation introduced in the current contribution is easier to handle since here we have to distinguish only between four cases whereas with the approximation of Rohr & Schnörr (1992) there are 16 cases.

7 Identification

For recovering corners in images we fit our parametric model directly to image intensities. Estimates for the model parameters $\vec{p} = (p_1, \ldots, p_n) \in \mathcal{R}^n$ are found by minimizing the squared differences between the (nonlinear) model function and the considered grey values:

$$\min_{\vec{p} \in \mathcal{R}^n} S(\vec{p}) \qquad (14)$$

where the objective function is given by

$$S(\vec{p}) = \|\vec{g} - \vec{g}_M(\vec{p})\|_2^2$$

$$= \sum_{i=1}^{m} \left(g(\vec{x}_i) - g_M(\vec{x}_i, \vec{p})\right)^2$$

The intensities and the function values of the model in the considered image area are $\vec{g} = \left(g(\vec{x}_1), \ldots, g(\vec{x}_m)\right)$ and $\vec{g}_M(\vec{p}) = \left(g_M(\vec{x}_1, \vec{p}), \ldots, g_M(\vec{x}_m, \vec{p})\right) \in \mathcal{R}^m$, respectively. For getting first experimental results, in Rohr (1990, 1992) we used the downhill method of Powell (1964) utilizing only function values. Here, in order to reduce the computation time, we apply the method of Levenberg-Marquardt (Marquardt 1963) incorporating partial derivatives of the model function in (8). An initial parameter vector $\vec{p}_0$ for the iteration is determined using local operations (see Rohr 1990, 1992). It should be noted that the identification result relies on the initial parameter values and as usual with nonlinear cost functions in general we cannot guarantee to find the global minimum. However, in our experiments the initial values turned out to be sufficiently good.

8 Recognition of Deviations from the Model

The foregoing identification procedure is applied directly to the original image as well as—for reasons of noise reduction—to the image smoothed with a Gaussian filter, where we choose the filter values as $\sigma_F = 0$ (no filtering) and $\sigma_F = 0.5$, 1.0, and 1.5. Smoothing the original image increases the widths of the grey-value transitions. If we assume the transitions in the image to be describable by an amount of blur of σ_0 then the blur of the smoothed original image is given by $\sigma = \sqrt{\sigma_0^2 + \sigma_F^2}$. Thus, the width of the grey-value transitions in the original image can be evaluated by

$$\sigma_0 = \sqrt{\sigma^2 - \sigma_F^2} \tag{15}$$

If the considered grey-value structure in the image agrees with the model then the estimated model parameters should be (nearly) independent of smoothing the image beforehand. The mean values of the determined parameters for the different values of σ_F could be taken as estimates for the parameters. On the other hand, observing large variations in the parameter values for different amounts of Gaussian smoothing suggests that the employed model is inadequate. This can be due to interaction effects from other prominent features or for reasons that a single grey-value structure deviates from the assumed model. Whereas in the first case the considered area should be decreased, a different model should be used in the second case. Another cue for checking the validity of the model is the mean-squared difference between the model and the intensities.

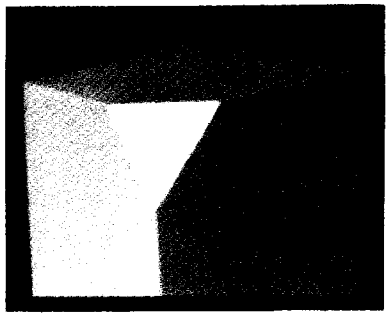

Fig. 13. Grey-value image of a cut cube.

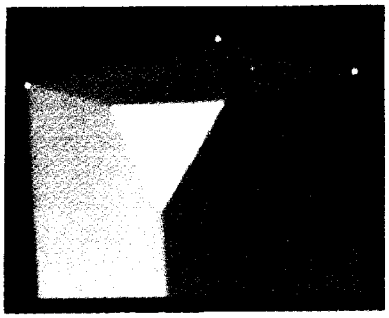

Fig. 14. Detected corners of figure 13.

9 Experimental Results

In this section we show identification results of our approach for real image data. Since the general model also comprises straight step edges we show experimental results of such edges, too. Model fitting approaches for straight step edges are also introduced by Hueckel (1971, 1973) and Nalwa and Binford (1986). However, these approaches have been designed for straight edges but not for corners. Applying our approach to an approximately 20×20 portion of the image of the step edge marked in figure 15 (the profile of this step edge is displayed in figure 16) we get the identification results shown in table 1 which approximate the original step edge fairly well. The estimated model parameters, the mean error $\bar{e}$ (positive root of the mean squared error),

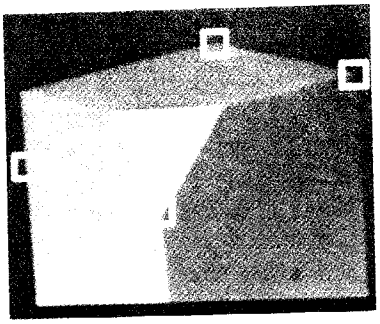

Fig. 15. Considered features of figure 13.

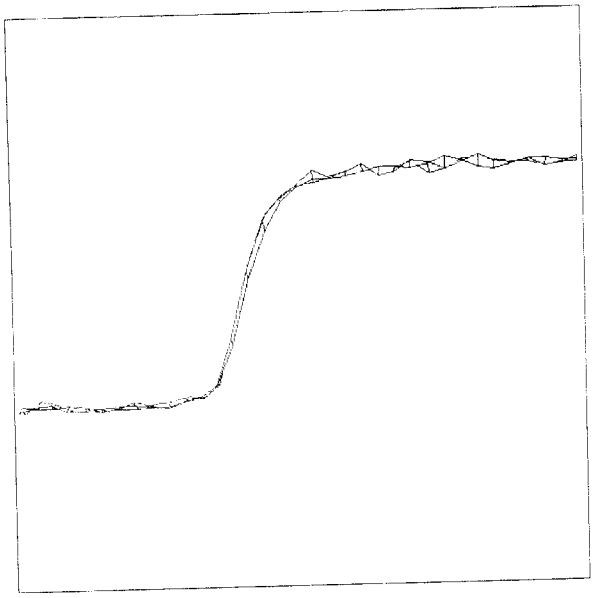

Fig. 16. Profile of the step edge marked in figure 15.

and the estimates for the blur in the unfiltered image σ_0 using (15) are given in this table, where the value of σ_F characterizes the amount of smoothing of the original image with a Gaussian filter before the model is fit to the intensities. We see that the more we smooth (increasing σ_F) the better is the agreement of the image with the model function (decreasing $\bar{e}$). This is because smoothing the original image reduces the noise. It can also be observed that with the exception of the expected increase of σ, the estimated model parameters are nearly independent of σ_F, that is, it is possible to first smooth the original image in order to reduce the noise before applying the identification procedure.

For some further tests of our approach on other images we refer to Bergholm and Rohr (1991), where the estimates for the width and height of step edges were compared with the estimates of the approach of Zhang and Bergholm (1991). One interesting example is the asymmetric step edge shown in figure 17 for which the two approaches yielded different results. For both approaches the assumptions are violated. Considering the identification results of our approach in table 2, we can observe that some of the estimated model parameters vary in dependence of the amount of filtering σ_F. Especially, the paramter σ_0, which characterizes the width of the transition, increases very much. This is an indication that the underlying model is not adequate. We also see that the mean error $\bar{e}$ for this asymmetric step edge is much larger than the one of the nearly symmetric step edge in table 1. This observation gives an idea of how our approach can be used to check the validity of the parametric model. When verifying this for a larger number of experiments a statistical test should be used.

Next we discuss the identifcation results of the L-corner in figure 15 (figure 13 is the original image and the detected corner positions used as starting values for the minimization procedure are shown in figure 14). For the identification of step edges the model function is explicitly given by $\phi(x)$. For corners, however, we use the approximation of the model developed in section 6. Applying the minimization method of Levenberg-Marquardt (Marquardt 1963) in a 25×25 image area, we get the results listed in table 3. As for the step edge in our first example it can be observed that the estimated parameters are nearly independent of smoothing the image beforehand. This is also true for the position $\vec{x}_0$ of the corner, because $\vec{x}_0$ indicates the origin of the grey-value structure, that is, the position of the unsmoothed

Table 1. Identification result of the step edge in figures 15 and 16.

σ_F	x_0	α	a_0	a_1	σ	$\bar{e}$	σ_0
0.0	11.87	3.87	16.15	115.09	1.52	2.48	1.52
0.5	11.87	3.97	16.13	114.92	1.59	1.98	1.51
1.0	11.86	4.27	16.25	114.03	1.82	1.02	1.52
1.5	11.89	4.24	16.08	114.66	2.13	0.60	1.52

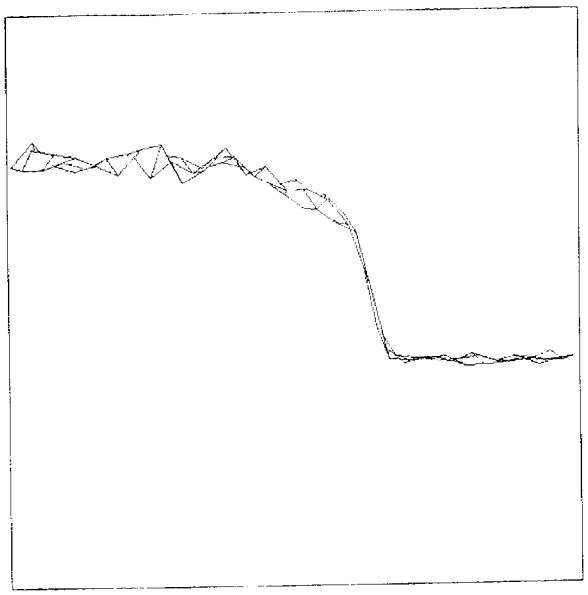

Fig. 17. Asymmetric step edge.

corner (for the model parameter $\sigma = 0$). Under the assumption that 3D-edges are very sharp and that the blur of the imaging system is approximately describable by Gaussian convolution our approach helps to reduce the influence of the blur of the imaging system. This is especially important for determining the position of features when the distances of objects in the scene to the recording camera differ very much or when the camera is not well focused. The estimate for the width of the grey-value transitions is $\sigma_0 \approx 1.0$ and is much smaller than the one for the step edge ($\sigma_0 \approx 1.5$) in the first example. This is plausible since the L-corner is in the rear of the recorded object and therefore the transitions are represented by a smaller number of pixels than the transitions of the step edge which is closer to the recording camera. For comparison we also show the identification results for this L-corner with our previous approach Rohr (1990, 1992) (numerical integration to compute the model and minimization with the method of Powell (1964)) in table 4. With the new approach, which reduces the computation time from several hours to a few minutes on a DEC Station 2000 (implemented in Ada), the estimated parameters are nearly the same. The differences of the results to our previous approach lie within the parameter variations in dependence of σ_F.

The application of the approach in the current distribution for the Y-corner in figure 15 yields the values in table 5. The estimates are also nearly independent of smoothing the image before fitting the model. Especially the determination of the position $\vec{x}_0$ is very stable. The original grey-value structure in figure 18 is fairly well approximated by the identified model in figure 19. From the estimated model parameters the edges of the depicted image can be reconstructed (see figure 20). In contrast to the original grey-value edges (see figure 3 and the dashed lines in figure 21), the reconstructed edges are closed, that is, there are no gaps, and the corner point is uniquely determined. Notice, that the highest plateau of the Y-corner is corrupted with a more or less elliptic region. Since our approach acts rather globally (i.e., we fit a model to the whole grey-value structure) such "microstructures" as well as noise do not affect the result very much. Local operators, however, in general have more difficulties with such influences.

Table 2. Identification result of the asymmetric step edge in figure 17.

σ_F	x_0	α	a_0	a_1	σ	$\bar{e}$	σ_0
0.0	138.62	59.10	200.26	64.06	1.08	9.19	1.08
0.5	138.53	59.20	201.05	63.69	1.31	7.34	1.21
1.0	138.40	59.01	201.97	62.90	1.75	4.40	1.44
1.5	138.33	58.91	203.70	61.60	2.22	2.61	1.63

Table 3. Identification result of the L-corner in figure 15.

σ_F	x_0	y_0	α	β_1	a_0	a_1	σ	$\bar{e}$	σ_0
0.0	27.19	28.60	267.71	158.64	15.30	64.10	0.99	1.61	0.99
0.5	27.22	28.60	267.68	159.28	15.30	63.99	1.09	1.04	0.97
1.0	27.24	28.46	267.87	159.86	15.33	63.84	1.42	0.42	1.01
1.5	27.24	28.40	267.96	159.83	15.28	63.91	1.78	0.24	0.95

Table 4. Identification result of the L-corner in figure 15 with our previous approach.

σ_F	x_0	y_0	α	β_1	a_0	a_1	σ	$\bar{e}$	σ_0
0.0	27.18	28.60	267.72	158.33	15.33	64.12	0.96	1.60	0.96
0.5	27.22	28.64	267.63	159.17	15.32	64.01	1.09	1.03	0.97
1.0	27.24	28.50	267.82	159.65	15.35	63.87	1.42	0.43	1.01
1.5	27.23	28.39	267.96	159.34	15.30	63.95	1.78	0.26	0.96

Table 5. Identification result of the Y-corner in figure 15.

σ_F	x_0	y_0	α	β_1	β_2	a_0	a_1	a_2	σ	$\bar{e}$	σ_0
0.0	29.66	26.26	91.17	58.85	145.76	124.41	177.62	59.66	1.48	2.90	1.48
0.5	29.70	26.21	90.96	58.41	145.18	124.33	178.06	59.83	1.56	2.44	1.48
1.0	29.72	26.20	91.27	58.67	144.81	124.07	178.87	59.71	1.88	1.75	1.59
1.5	29.79	26.17	91.02	57.87	144.58	124.13	179.84	59.35	2.20	1.20	1.62

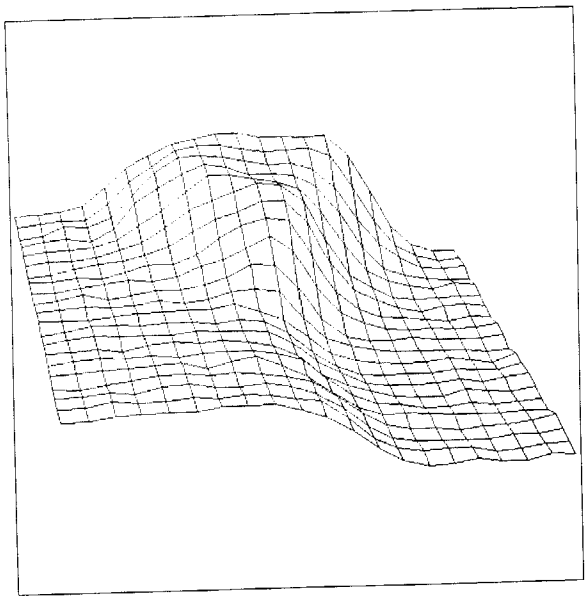

Fig. 18. 3D-plot of the Y-corner marked in figure 15.

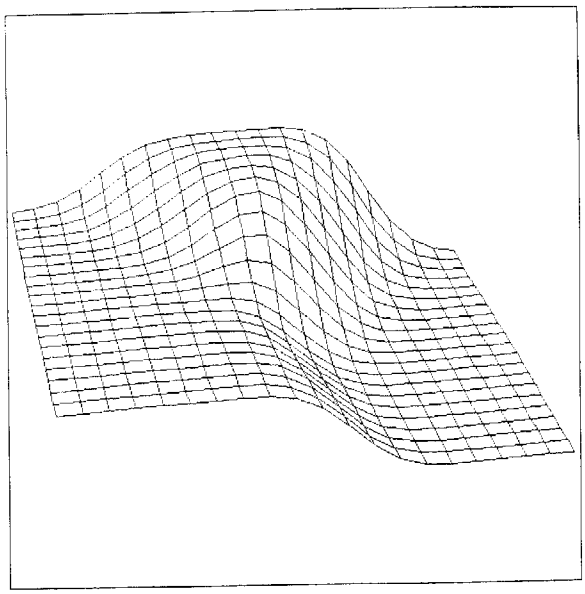

Fig. 19. Identified model of the Y-corner in figure 18.

For the ARROW-corner marked in figure 15 the estimates in table 7 are also nearly independent of smoothing with the exception of the slight decrease of β_1 and σ_0. This indicates that the underlying model in this case deviates a bit. However, by increasing the area where the model is fit to the image, the variation of the two parameters can be reduced which also means that this area was not chosen carefully. The choice of the window size is a crucial problem especially when other image features are very close to the considered grey-value structure. Automatically choosing the window size is still an open question. For comparison the estimates with our previous approach are given, too (see tables 6 and 8).

We also show identification results for the features marked in figure 24 (see also figures 22 and 23). The estimates for the considered L-, Y-, and ARROW-corner are listed in tables 9, 10, 11 and again demonstrate the efficiency of our approach.

10 Conclusion and Further Work

Starting from the parametric model of Rohr (1990, 1992), we have introduced here an approach for the identification of a certain class of prominent features in grey-value images comprising step edges, L-corners,

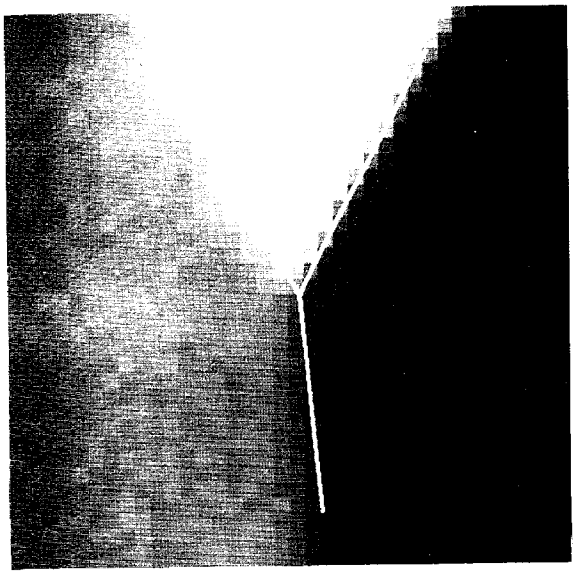

Fig. 20. Reconstructed edges for the Y-corner in figure 18.

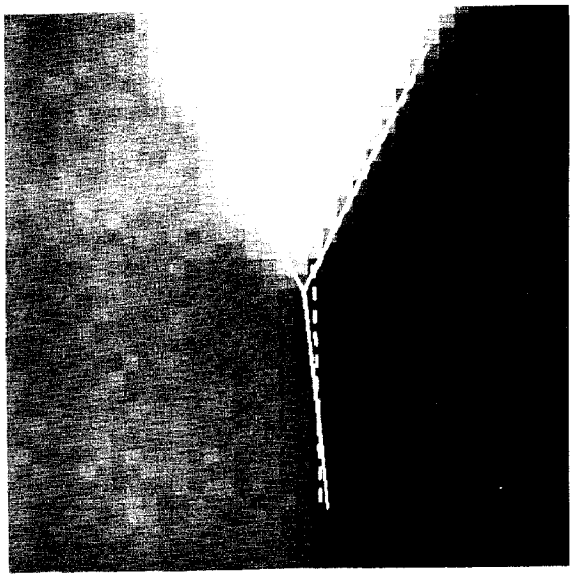

Fig. 21. Comparison of reconstructed edges (solid lines) and grey-value edges (dashed lines).

Table 6. Identification result of the Y-corner in figure 15 with our previous approach.

σ_F	x_0	y_0	α	β_1	β_2	a_0	a_1	a_2	σ	$\bar{e}$	σ_0
0.0	29.60	26.30	91.42	59.31	146.00	124.41	177.50	59.66	1.46	2.87	1.46
0.5	29.65	26.25	91.19	58.88	145.40	124.32	177.97	59.82	1.55	2.41	1.46
1.0	29.69	26.20	91.17	58.70	144.56	124.09	179.05	59.66	1.87	1.69	1.58
1.5	29.68	26.23	91.30	58.50	145.17	124.15	179.72	59.38	2.18	1.15	1.58

Table 7. Identification result of the ARROW-corner in figure 15.

σ_F	x_0	y_0	α	β_1	β_2	a_0	a_1	a_2	σ	$\bar{e}$	σ_0
0.0	21.84	32.01	230.21	68.66	30.99	12.92	42.13	68.98	1.01	2.48	1.01
0.5	21.84	32.07	229.65	67.14	31.09	12.86	42.14	69.08	1.10	2.16	0.99
1.0	21.81	32.15	228.63	64.18	31.41	12.72	42.29	69.08	1.40	1.75	0.98
1.5	21.76	32.22	228.39	63.34	31.34	12.69	42.36	68.91	1.72	1.44	0.84

Table 8. Identification result of the ARROW-corner in figure 15 with our previous approach.

σ_F	x_0	y_0	α	β_1	β_2	a_0	a_1	a_2	σ	$\bar{e}$	σ_0
0.0	21.85	32.00	230.15	68.53	31.01	12.93	42.10	69.01	1.00	2.47	1.00
0.5	21.84	32.03	229.80	67.36	31.16	12.88	42.15	69.10	1.10	2.15	0.98
1.0	21.82	32.13	228.58	64.14	31.43	12.76	42.30	69.10	1.40	1.73	0.97
1.5	21.77	32.16	228.51	63.56	31.45	12.76	42.34	68.95	1.72	1.41	0.83

T-, Y-, ARROW-corners, and more complex junction types. With this two-dimensional model the underlying assumptions are made explicit, while most existing approaches implicitly suppose special grey-value functions. By fitting our model directly to image intensities this approach not only determines the position of grey-value structures to subpixel resolution but also yields additional attributes such as the width of the grey-value

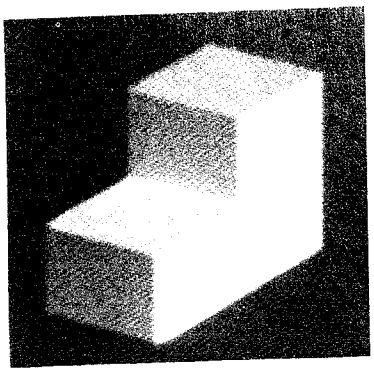

Fig. 22. Grey-value image.

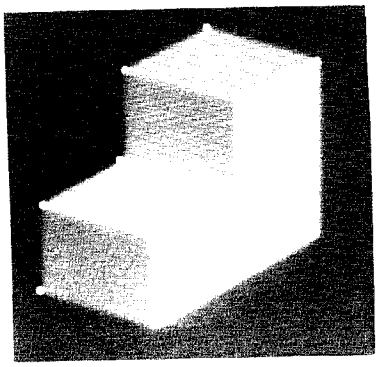

Fig. 23. Detected corners of figure 22.

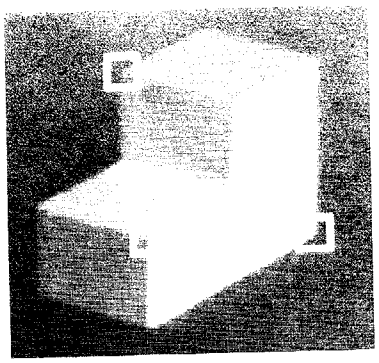

Fig. 24. Considered features of figure 22.

transitions. Assuming ideal sharp 3D-edges and Gaussian blur of the imaging system we here have a possibility to estimate as corner position the origin of the ideal unsmoothed grey-value structures, that is, to reverse the blur. Therefore, when the underlying assumptions of the model are fulfilled our approach does not suffer from the displacement of the corner position caused by the blur of the imaging system and by other smoothing operations. This is an advantage over approaches that define the L-corner position as the point of maximal planar curvature in the line with steepest slope. For those approaches we have derived an implicit equation describing their localization error compared

Table 9. Identification result of the L-corner in figure 24.

σ_F	x_0	y_0	α	β_1	a_0	a_1	σ	$\bar{e}$	σ_0
0.0	166.69	204.89	147.50	121.72	15.24	136.12	1.49	3.32	1.49
0.5	166.71	204.87	147.37	122.08	15.22	136.12	1.57	2.98	1.49
1.0	166.75	204.79	146.98	123.55	15.05	136.24	1.83	2.11	1.54
1.5	166.77	204.81	147.06	123.44	14.69	136.44	2.14	1.61	1.53

Table 10. Identification result of the Y-corner in figure 24.

σ_F	x_0	y_0	α	β_1	β_2	a_0	a_1	a_2	σ	$\bar{e}$	σ_0
0.0	165.48	99.45	329.61	118.61	104.15	93.69	138.90	54.17	1.52	2.35	1.52
0.5	165.48	99.45	329.80	118.74	103.91	93.66	138.88	54.33	1.60	2.14	1.52
1.0	165.49	99.43	330.48	118.66	103.94	93.46	138.78	54.61	1.84	1.62	1.55
1.5	165.48	99.42	330.49	118.45	104.15	93.46	139.01	54.29	2.16	1.22	1.56

Table 11. Identification result of the ARROW-corner in figure 24.

σ_F	x_0	y_0	α	β_1	β_2	a_0	a_1	a_2	σ	$\bar{e}$	σ_0
0.0	59.13	83.60	2.57	48.02	68.91	11.28	83.08	56.72	1.24	1.46	1.24
0.5	59.12	83.62	2.35	48.36	68.72	11.30	83.10	56.57	1.33	1.25	1.23
1.0	59.08	83.62	1.91	48.84	68.03	11.30	83.12	56.24	1.63	0.88	1.29
1.5	59.05	83.63	1.81	48.63	68.00	11.20	83.53	56.44	1.97	0.67	1.28

to the origin of the ideal unsmoothed grey-value structure. Another advantage of our approach is that it acts rather globally which means that small deformations of the image surface (in general) do not affect the estimation result as much as mere local approaches do.

When an analytical approximation to the model function is used and the minimization method of Levenberg-Marquardt is applied, the computational expense in comparison to that of our previous approach is reduced remarkably while nearly the same experimental results for real image data are obtained. In addition, we indicated that by fitting our model to the original as well as to the smoothed original image cues can be obtained for recognizing deviations from the model. This observation has to be verified experimentally in a larger number of experiments. Another issue that requires further attention is the automatic choice of the window size for the fit. In summary, we have sketched a unifying framework for the recognition of step edges and corners of a certain class. Extensions of this class are the generalization to curved edges and increasing (decreasing) plateaus of the ideal grey-value structures.

Acknowledgment

I'm very grateful to C. Schnörr and J. Rieger for discussions. For critical comments I thank F. Bergholm, K. Daniilidis, A. Korn, and Prof. G. Winkler. I also thank the reviewers for their helpful suggestions.

References

Abramowitz, M., and Stegun, I.A. 1965. *Handbook of Mathematical Functions:* Dover Publications: New York

Beaudet, P.R. 1978. Rotationally invariant image operators, *Proc. Intern. conf. Patt. Recog.* Kyoto/Japan, pp. 579–583, November.

Bergholm, F. 1987. Edge focusing, *IEEE Trans. Patt. Anal. Mach. Intell.* 9:726–741.

Bergholm, F., and Rohr, K. 1991. A comparison between two approaches applied for estimating diffuseness and height of step edges, Hausbericht Nr. 10262, Fraunhofer-Institut für Informations- und Datenverarbeitung (IITB), Karlsruhe/FRG; and Tech. Rept. TRITA-NA-P9105, CVAP 83, Dept. of Num. Analysis and Comput. Science, Royal Institute of Technology, Stockholm. March.

Berzins, V. 1984. Accuracy of Laplacian edge detectors, *Comput. Vis. Graph. Image Process.* 27:195–210.

Beymer, D.J. 1991. Finding junctions using the image gradient, *Proc. Conf. Comput. Vis. Patt. Recog.*, Maui, Hawaii, June 3–6, pp. 720–721.

Bronstein, I.N., and Semendjajew, K.A. 1981. *Taschenbuch der Mathematik*, 19. Auflage, Verlag Harri Deutsch, Thun und Frankfurt/Main.

Canny, F. 1986. A computational approach to edge detection, *IEEE Trans. Patt. Anal. Mach. Intell.* 8:679–698.

Deriche, R., and Giraudon, G. 1990. Accurate corner detection: An analytical study, *Proc. 3rd Intern. Conf. Comput. Vis.* Dec. 4–7, Osaka/Japan, pp. 66–70, December.

Dreschler, L., and Nagel, H.-H. 1981. Volumetric model and 3D-trajectory of a moving car derived from monocular TV-frame sequences of a street scene, *Proc. Intern. Joint Conf. Artif. Intell.*, Vancouver, pp. 692–697; see also *Comput. Graph. Image Process.* 20:199–228, 1982.

Förstner, W. 1986. A feature based correspondence algorithm for image matching, *Intern. Arch. Photogrammetry Remote Sens.* 26(3/3):150–166.

Giraudon, G., and Deriche, R. 1991. On corner and vertex detection, *Proc. Conf. Comput. Vis. Patt. Recog.*, Maui, Hawaii, pp. 650–655, June.

Guiducci, A. 1988. Corner characterization by differential geometry techniques, *Patt. Recog. Lett.* 8:311–318.

Hueckel, M.H. 1971. An operator which locates edges in digitized pictures, *J. Assoc. Comput. Mach.* 18(1):113–125.

Hueckel, M.H. 1973. A local visual operator which recognizes edges and lines, *J. Assoc. Comput. Mach.* 20(4):634–647.

Kitchen, L., and Rosenfeld, A. 1982. Gray-level corner detection, *Patt. Recog. Lett.* 1:95–102.

Korn, A. 1988. Towards a symbolic representation of intensity changes in images, *IEEE Trans. Patt. Anal. Mach. Intell.* 10: 610–625.

Li, D., Sullivan, G.D., and Baker, K.D. 1989. Edge detection at junctions, *Proc. 5th Alvey Vision Conf.*, University of Reading, Reading/UK, pp. 121–125, September.

Marquardt, D. 1963. An algorithm for least-squares estimation of nonlinear parameters, *J. Soc. Indust. Appl. Math.* 11:431–441.

Marr, D., and Hildreth, E. 1980. Theory of edge detection, *Proc. Roy. Soc. London* B 207:187–217.

De Micheli, E., Caprile, B., Ottonello, P., and Torre, V. 1989. Localization and noise in edge detection, *IEEE Trans. Patt. Anal. Mach. Intell.* 11:1106–1117.

Nalwa, V.S., and Binford, T.O. 1986. On detecting edges, *IEEE Trans. Patt. Anal. Mach. Intell.* 8(6):699–714.

Noble, J.A. 1987. Finding corners, *Proc. 3rd Alvey Vision Conf.*, University of Cambridge, Cambridge/UK, pp. 267–274, September.

Powell, M.J.D. 1964. An efficient method for finding the minimum of a function of several variables without calculating derivatives, *Computer Journal* 7:155–162.

Press, W.H., Flannery, B.P., Teukolsky, S.A., and Vetterling, W.T. 1988. *Numerical Recipes*, Cambridge University Press, Cambridge and New York.

Rangarajan, K., Shah, M., and Van Brackle, D. 1989. Optimal corner detector, *Comput. Vis. Graph. Image process.* 48:230–245.

Rohr, K. 1990. Über die Modellierung und Identifikation charakteristischer Grauwertverläufe in Realweltbildern, *12. DAGM—Symposium Mustererkennung*, September, Oberkochen-Aalen, Informatik-Fachberichte 254, R.E. Großkopf (Hrsg.), Sprinter-Verlag Berlin Heidelberg, pp. 217–224.

Rohr, K. 1992. Modelling and identification of characteristic intensity variations, *Image Vis. Comput.* 10(2):66–76.

Rohr, K., and Schnörr, C. 1992. An efficient approach for identification of characteristic intensity variations, Tech. Rept. FBI-HH-M-242/92, FB Informatik, Universität Hamburg.

Waltz, D. 1975. Understanding line drawings of scenes with shadows. in *The Psychology of Computer Vision*, P.H. Winston (ed.), McGraw-Hill, New York, pp. 19–91.

Zhang, W., and Bergholm, F. 1991. An extension of Marr's "signature" based edge classification, *7th Scandinavian Conf. Image Anal.*, Aalborg/Denmark, August.

Zuniga, O.A., and Haralick, R.M. 1983. Corner detection using the facet model, *Proc. IEEE Conf. Comput. Vis. Patt. Recog.* Washington D.C., pp. 30–37, June 19–23.

Appendix I

Approximation of $\phi(x)$ for $0 \leq x \leq \infty$:

$$\phi(x) = 1 - (b_1 t + b_2 t^2 + b_3 t^3 + b_4 t^4 + b_5 t^5) G(x) + \epsilon(x) \qquad t = \frac{1}{1 + px}$$

$$|\epsilon(x)| < 7.5 \cdot 10^{-8}$$

	1530		3782
	7937		5978
	4429		19
$b_1 =$	0.31938	$b_2 =$	−0.35656
$b_3 =$	1.78147	$b_4 =$	−1.82125
$b_5 =$	1.33027	$p =$	0.23164

Appendix II

Coefficients for (13) using $d = (ht)^4$:

$-2h \leq x \leq -h$:

$$c = 2ht + \zeta_2,$$

$$c_1 = c^3/6d,$$

$$c_2 = c^2/4d,$$

$$c_3 = c/6d,$$

$$c_4 = 1/24d$$

$-h \leq x \leq 0$:

$$c = 2ht + \zeta_2,$$

$$c_1 = \frac{4/3(ht)^3 - c\zeta_2^2}{2d},$$

$$c_2 = -\frac{\zeta_2(\zeta_2 + 2c)}{4d},$$

$$c_3 = \frac{2\zeta_2 + c}{6d},$$

$$c_4 = -\frac{1}{8d}$$

$0 \leq x \leq h$:

$$c = 2ht - \zeta_2,$$

$$c_1 = \frac{4/3(ht)^3 - c\zeta_2^2}{2d},$$

$$c_2 = \frac{\zeta_2(\zeta_2 - 2c)}{4d},$$

$$c_3 = \frac{2\zeta_2 - c}{6d},$$

$$c_4 = \frac{1}{8d}$$

$h \leq x \leq 2h$:

$$c = 2ht - \zeta_2,$$

$$c_1 = c^3/6d,$$

$$c_2 = -c^2/4d,$$

$$c_3 = c/6d,$$

$$c_4 = -1/24d.$$